CrossMark

RESEARCH PAPER

Microfluidic separation of magnetic particles with soft magnetic microstructures

Ran Zhou[1] · Cheng Wang[1]

Abstract This paper demonstrates simple and cost-effective microfluidic devices for enhanced separation of magnetic particles by using soft magnetic microstructures. By injecting a mixture of iron powder and polydimethylsiloxane (PDMS) into a prefabricated channel, an iron–PDMS microstructure was fabricated next to a microfluidic channel. Placed between two external permanent magnets, the magnetized iron–PDMS microstructure induces localized and strong forces on the magnetic particles in the direction perpendicular to the fluid flow. Due to the small distance between the microstructure and the fluid channel, the localized large magnetic field gradients result a vertical force on the magnetic particles, leading to enhanced separation of the particles. Numerical simulations were developed to compute the particle trajectories and agreed well with experimental data. Systematic experiments and numerical simulation were conducted to study the effect of relevant factors on the transport of superparamagnetic particles, including the shape of iron–PDMS microstructure, mass ratio of iron–PDMS composite, width of the microfluidic channel, and average flow velocity.

✉ Cheng Wang
wancheng@mst.edu

[1] Department of Mechanical and Aerospace Engineering, Missouri University of Science and Technology, 400 W. 13th St., Rolla, MO 65409, USA

1 Introduction

Magnetism and magnetic particles or beads have long been used for bioseparation applications in biomedical sciences and clinical medicines (Safarik and Safarikova 1999, 2004). For example, immunomagnetic separation (IMS) is a standard laboratory technique for isolating cells, proteins, and nucleic acids. In this technique, magnetic particles conjugated with antibodies bind to antigens of the targeted cells' surface and thus allow the cells to be isolated, purified, and collected with a magnetic force field. Quadrupole magnetic flow sorter (QMS) has been used for isolation of cancer cells from patients with head and neck cancer (Yang et al. 2009; Balasubramanian et al. 2012) and to separate islet cells for diabetes diagnosis research (Shenkman et al. 2009). Lund-Olesen et al. studied the hybridization of target DNA in solution with probe DNA on magnetic beads immobilized on the channel sidewalls in a magnetic bead separator (Lund-Olesen et al. 2007b).

Over the last decade, magnetism has been integrated with microfluidics to harness the advantages of miniaturization, automation, and integration, and the term "magnetofluidics" has been coined (Verpoorte 2003; Gijs 2004; Pamme 2006; Gijs et al. 2009; Nguyen 2012; Hejazian et al. 2015). Microfluidic-based magnetophoretic techniques have been demonstrated in continuous separation of erythrocytes and leukocytes from whole blood (Han and Bruno Frazier 2004) and *E. coli* bacteria from living cells (Xia et al. 2006). The use of magnetofluidics for bioseparation has received growing interest due to a number of unique advantages: low cost, insensitivity to temperature or pH, and remote actuation without direct contact. In some applications, magnetofluidics are favored over other methods, such as acoustic, electric, and optical forces, which often involve complex designs or strongly depend on the

properties of the flow medium or the interaction between the fluid and fluidic channels (Pamme 2006; Gijs et al. 2009; Nguyen 2012).

The simplest and most prominent class of microsystems for magnetic particle separation relies on the combination of microstructures made of soft magnetic materials and an externally applied magnetic field. This combination offers a number of benefits. First, the magnetic strength can be easily adjusted or removed by controlling the strength of the external magnets. Second, due to their small size, the magnetized microstructures can provide strong magnetic field gradients and thus large forces, leading to efficient capture of magnetic particles. This is similar to traditional high-gradient magnetic separators (HGMSs) (Lin et al. 2007) used for large-scale magnetic separation, which comprise a separation column filled with a steel wool matrix in a large external magnetic field (Svoboda 2001; Watson 1973).

Several methods have been reported in the literature on integrating microstructures with microfluidics to increase the local magnetic gradients (Do et al. 2004; Deng et al. 2002; Rida and Gijs 2004; Lund-Olesen et al. 2007a; Furlani and Ng 2006; Smistrup et al. 2005; Furlani and Sahoo 2006). Micrometer-scale metal structures, such as pillars and strips, have been fabricated or patterned inside microfluidic channels (Deng et al. 2002; Inglis et al. 2004; Xia et al. 2006). Once magnetized by a magnetic field from external permanent magnets, these microstructures of soft materials generated strong magnetic field gradients and efficiently trapped or deflected superparamagnetic beads moving past them in a flowing stream of sample fluid. Lin et al. injected a continuous flow of nickel microparticle suspensions into an auxiliary channel next to the main fluidic channel (Lin et al. 2007). The nickel microparticles were able to bend and concentrate the external magnetic field gradient. This magnetic field gradient induced magnetic forces on the particles in the main channel. Derec et al. built microfluidic channels on a copper PCB broad and applied electric current through etched copper circuits to induce local magnetic field (Derec et al. 2010). Faivre et al. studied the patterning of iron–PDMS composites inside microfluidic channels which could locally generate high gradients of magnetic field when exposed to external magnetic fields (Faivre et al. 2014).

In this paper, we present a simple and low-cost technique to fabricate microfluidic devices that integrate microstructures to increase the magnetic forces. The method is based on a microsolidics technique (Siegel et al. 2006; Tan et al. 2014). The magnetic microstructures are made by injecting and curing a mixture of iron powder and PDMS in a structural microchannel next to the fluidic channel. We investigated various factors that influence the sorting performance, including the shape of iron–PDMS microstructure, mass ratio of iron powder, microfluidic channel width,

and average flow velocity. We also developed a numerical method that can predict the particle separation and show good agreement with experimental measurements.

Compared to the existing methods, our method has several advantages. First, different iron mass ratios can be used to adjust the magnetic permeability and thus the magnetic forces. Second, the fluidic and structural channels are fabricated from a simple one-step soft-lithography process. It is flexible to design different shapes and sizes of the microstructure and place them within micrometer accuracy to the fluidic channel. Moreover, our method is particularly attractive for applications concerning biological objects (e.g., living cells), because the microstructures are situated outside the fluidic channels and will reduce the possibilities of contamination to the cells.

2 Concept and experiment

Figure 1a shows an overview of the microdevice, which consists of a fluidic channel and microstructures. The fluidic channel has two inlets and two outlets. External permanent magnets magnetize the soft magnetic structures to provide local magnetic field gradients, which in turn result in the deflection of magnetic particles. A magnetic particle exposed to a magnetic field experiences a magnetic force, F_m. The other important force acting on the particles is the hydrodynamic drag force F_d due to the surrounding fluid. The two forces, F_m and F_d, thus determine the movement of the magnetic particle.

The major steps of the fabrication process are summarized in Fig. 1a. Two channels, fluidic and structural, are first made in polydimethylsiloxane (PDMS) with soft-lithography technique (McDonald et al. 2000). A mixture of iron powder and PDMS in the liquid form is then injected into the structural channel and allowed to solidify. Figure 1b-1–b-3 shows the three different microstructure shapes: half circle, 60° isosceles triangle, and 120° isosceles triangle studied in this paper. These three structures are denoted as half circle, 60° triangle and 120° triangle hereinafter. The microstructures all have the same base length or diameter of 1000 μm. The nearest distance between the microstructures and the fluidic channel is $w_g = 60$ μm.

Shape selection In the current study, we emphasize on the flexibility of the proposed technique. We chose three representative shapes, half circle, 60° isosceles triangle, and 120° isosceles triangle, to show the influence of the shape, as shown in Fig. 1b. From prior works (Xia et al. 2006), it is known that soft magnetic microstructures of *half circle* and *triangle* shapes can generate strong magnetic fields to trap magnetic particles, so we selected these two shapes. Additionally, the magnetic force acting on particles is proportional to the magnetic field gradients mentioned in
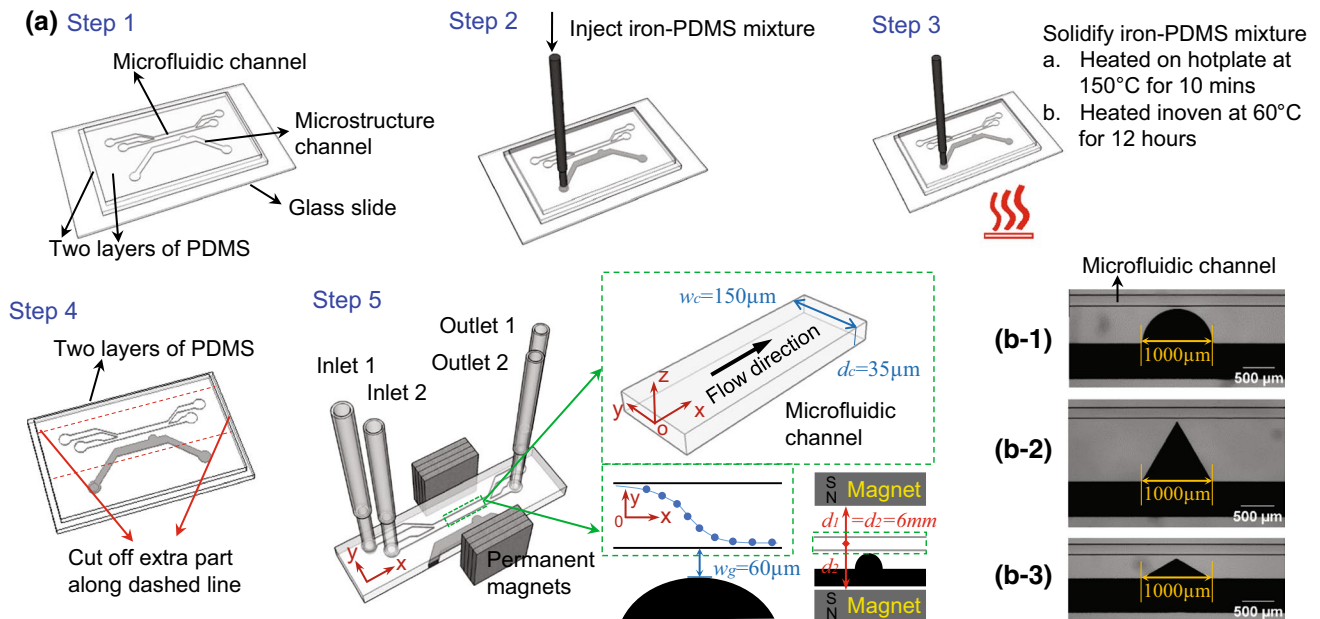
Fig. 1 Fabrication process of the microfluidic device. **a** The schematic illustration of the basic fabrication steps (not to scale). The microfluidic channel has a width $w_c = 150\,\mu m$ and a depth $d_c = 35\,\mu m$; the gap distance between the microstructure and the microfluidic channel is $w_g = 60\,\mu m$. **b-1**–**b-3** are the micro-photographies of the three different shapes for the microstructure: *half circle*, 60° isosceles triangle, and 120° isosceles triangle

Eq. (1), so we explored if a sharper angle can generate a larger magnetic field gradient thus a stronger magnetic force to attract particles. For these reasons, 60 and 120° triangles were chosen. Actually, there is a range of possible shapes to generate localized magnetic forces, e.g., square, rectangle, symmetric or asymmetric triangles. To find the 'best' shape for particle separation will require a systematic investigation and optimization.

Gap distance selection While the gap distance is one of the factors affecting magnetic separation, the gap distance was kept fixed at 60 microns in this study. This is because the effect of the gap distance w_g has been relatively well understood from previous study in the literature (Xia et al. 2006), and the results suggest that a closer distance of the magnetic microstructure from the microfluidic channel can generate larger magnetic forces. In this study, $w_g = 60\,\mu m$ was the closest distance we could achieve with a low-cost manufacturing technique, which we described in detail in a published work (Zhang et al. 2015). With conventional methods of producing master molds, e.g., SU-8 or deep reactive ion etching of silicon, the distance can be easily reduced to ten microns (McDonald et al. 2000).

In this study, we fabricated several microdevices to study the factors influencing the sorting performance. Two mass ratios of iron powder to PDMS were used in this study, at 1:1 to 2:1, respectively. The microfluidic channel width was designed to be $w_c = 150\,\mu m$ and 250 μm to study the effect of fluidic channel width.

2.1 Microfluidic device fabrication

The microfluidic device was fabricated in PDMS using a soft-lithography technique (McDonald et al. 2000). Master molds were manufactured in a dry film photoresist (MM540, 35 μm thick, DuPont) by lithographic patterning (Zhou and Wang 2015). A layer of dry film resist was first laminated onto a copper plate using a thermal laminator. After ultraviolet (UV) exposure through a transparency photo mask (10,000 dpi, CAD/Art Services Inc), the exposed dry film was developed, rinsed and dried to obtain the master mold. PDMS base and initiator were thoroughly mixed, degassed, and then cast on the master. After curing, the PDMS replica was peeled off from the master, cut and punched, and then bonded with another thin PDMS layer after corona surface treatment. Using this method, microfluidic and microstructure channels with rectangular cross-sectional shape were fabricated.

The PDMS device was placed onto a flat glass slide which served as a supporting substrate as displayed in step 1 of Fig. 1a. Next, carbonyl iron powders (C3518, Sigma-Aldrich) were thoroughly mixed with a premixed liquid PDMS. The mixture of the iron powders and PDMS was degassed, and subsequently injected into the microstructure channel with a syringe pump shown in step 2. Immediately after filling the iron–PDMS mixture, the microdevice was heated on a hotplate at 150°C for 10 min to cure the mixture, as in step 3 of Fig. 1a. The fast curing process

is critical to prevent the agglomeration and sedimentation of the iron powders, which have a density of 7.8 g/mL. The fast curing ensures a homogeneous distribution of the iron powders into the composite matrix. The microfluidic device was heated in an oven at 60 °C for another 12 hours to ensure complete curing and strong bonding. In step 4, excessive parts were cut off after curing of the iron–PDMS mixture.

The device was placed in the center of two pieces of parallel permanent magnets (Xia et al. 2006; Gelszinnis et al. 2013), as shown in step 5 of Fig. 1a. The separation distance of the permanent magnets was 12 mm. The placement at the center ensured a uniform external magnetic field in the microfluidic channel. Note that a uniform magnetic field has zero field gradients and thus will not cause a force on the magnetic particles. The nonzero magnetic field gradients are due to the magnetized iron–PDMS microstructures only, allowing us to study the effects of the soft magnetic microstructures on the sorting performance.

2.2 Materials

Micron-sized magnetic particles (MPS5UM, Magsphere) were used as model particles. The magnetic particles have a mean diameter of 5 μm, and are synthesized by embedding superparamagnetic iron oxide crystals into a polystyrene matrix. The particles have a density of 2.5 g/mL. The magnetic particles were suspended in 45.6% (w/w) aqueous glycerol solution whose viscosity is about 5 mPa·s. The larger viscosity reduced the particle sedimentation. The original solution of 5 μm superparamagnetic particles (2.5 % w/w) were diluted 500 times in the aqueous glycerol solution. The final particle concentration was 3.26×10^5/mL. The glycerol solution with magnetic particles was injected into inlet 1 as the particle solution, and 45.6 % glycerol solution was injected to inlet 2 as the buffer solution. Surfactant Tween 20 was added to both solutions at a concentration of 0.5 % w/w to prevent particle adhesion to channel walls and particle agglomeration.

2.3 Experimental setup

The microdevice was placed on an inverted microscope stage (IX73, Olympus). Four pieces of $1'' \times 1'' \times \frac{1}{8}''$ thick permanent magnets (BX0X02, KJ Magnetics, Inc.) were placed symmetrically on each side of the microdevice, in Fig. 1a. The microfluidic devices were illuminated by a fiber optic light for transmission bright-field imaging. The flow rates to the inlets were controlled separately by two syringe pumps (NE-300, New Era and KDS 200, KDS Scientific). To maintain good stability of the flow, small syringes (1 mL) were used to minimize the effect of the

motor's step motion. To record particle trajectories, a high-speed camera (Phantom Miro M310, Vision Research) was used to capture videos. In experimental data analysis, ImageJ (Abramoff et al. 2004) was used to extract the particle trajectory, from which the translational velocity v_p and the vertical position z_p can be calculated.

3 Theory and simulation

3.1 Force analysis of magnetic particles

Magnetic force Exposed to a magnetic field, a magnetic particle experiences a magnetic force, $\mathbf{F}_m$, which is expressed as (Engel and Friedrichs 2002)

$$\mathbf{F}_m = \mu_0 \int_V (\mathbf{M} \cdot \nabla)\mathbf{H} dV, \tag{1}$$

where $\mu_0 = 4\pi \cdot 10^{-7} H \cdot m^{-1}$, is the vacuum permeability; $\mathbf{H}$ is the magnetic field intensity; $\mathbf{M}$ is the field-dependent particle magnetization; V is the volume. In a static magnetic field, $\mathbf{H}$ and $\mathbf{M}$ are colinear, $\mathbf{M} = M(H)\frac{\mathbf{H}}{H} = M(H)\mathbf{e_H}$, where H and M are the magnitudes of $\mathbf{H}$ and $\mathbf{M}$, respectively, and $\mathbf{e_H} \equiv \mathbf{H}/H$ is a unit vector indicating the direction of the applied magnetic field.

Assuming a small variation of the integrand over magnetic particles, equation (1) can be written as (Smistrup et al. 2008)

$$\mathbf{F}_m \simeq V_p M_p \mathbf{G}, \tag{2}$$

where V_p is the volume of the magnetic particle and $\mathbf{G}$ is the magnetic field gradient in the direction of $\mathbf{H}$, given by

$$\mathbf{G} = \mu_0 (\mathbf{e_H} \cdot \nabla)\mathbf{H}. \tag{3}$$

Thus, the magnetic force on a magnetic particle is the product of the particle magnetic moment, $V_p M_p$, and $\mathbf{G}$, which is referred to as the effective magnetic field gradient (Smistrup et al. 2008).

The external magnetic field at the center of the parallel magnets was approximately 0.23 T, and its corresponding magnetization of pure Fe_3O_4 material is $M = 1.9 \times 10^5$ A/m according to the magnetization curve (Nguyen and Pho 2014).

Note that the magnetic particle used in this study is composed of a Fe_3O_4 core and an external polymer matrix. If the entire particle volume V_p is used to compute the force, an equivalent M_p accounting for the non-magnetic polymer volume must be used accordingly. The equivalent magnetization of the superparamagnetic particles is therefore $M_p = M \frac{V_m}{V_p}$, where $\frac{V_m}{V_p}$ stands for the volume ratio of the Fe_3O_4 core to the entire particle volume. Based on the data sheet provided by the manufacturer, we calculated the

value of $M_p \approx 11000$ A/m. In addition, our numerical simulations also confirmed the accuracy of M_p.

Stokes drag force In low Reynolds number microfluidic systems, the dominating force acting on particles from the fluid is the hydrodynamic drag force $\mathbf{F_d}$ defined by Stokes' law (Zhu et al. 2010),

$$\mathbf{F_d} = 3\pi\eta D(\mathbf{v_f} - \mathbf{v_p})f_D \tag{4}$$

where η is the fluid viscosity, $\mathbf{v_p}$ is the particle velocity, and $\mathbf{v_f}$ is the velocity of suspending fluid, and f_D is the hydrodynamic drag force coefficient. The coefficient, f_D, accounts for the increased fluid resistance when the particle moves near the microfluidic channel surface (Ganatos et al. 1980; Staben et al. 2003; Krishnan and Leighton 1995). It has a form of

$$f_D = \left[1 - 0.6526\left(\frac{D}{D+2z'}\right) + 0.1475\left(\frac{D}{D+2z'}\right)^3 \right. \\ \left. -0.131\left(\frac{D}{D+2z'}\right)^4 - 0.0644\left(\frac{D}{D+2z'}\right)^5 \right]^{-1}, \tag{5}$$

where z' is the distance between the bottom of the particle and the channel surface.

Velocity profile in rectangular microchannels The velocity profile of laminar steady flows in rectangular channels can be expressed as an infinite sum of Fourier series (White 1991). To improve the computational speed, we used an algebraic approximation of the following form for channel aspect ratio $\alpha = d_c/w_c \leq 0.5$ (Shah et al. 1978),

$$v(y,z) = v_{\max}\left[1 - \left(\frac{2y}{w_c}\right)^m\right]\left[1 - \left(\frac{2z}{d_c}\right)^n\right]. \tag{6}$$

Natarajan and Lakshmanan (Shah et al. 1978) solved the $N-S$ momentum equation by a finite element method and matched the velocity profile to the empirical equation to arrive at two flow parameters m and n as

$$m = 1.7 + 0.5\alpha^{-1.4} \tag{7}$$

$$n = \begin{cases} 2 & \text{for } \alpha <= \frac{1}{3} \\ 2 + 0.3\left(\alpha - \frac{1}{3}\right) & \text{for } \alpha >= \frac{1}{3} \end{cases} \tag{8}$$

The values of m and n by Natarajan and Lakshmanan yield profiles that are in good agreement with the experimental results of Holmes and Vermeulen (Shah et al. 1978).

The channel dimensions in this study are: the depth of microchannel $d_c = 35\,\mu m$, and the width of microfluidic channel $w_c = 150$ or $250\,\mu m$. The aspect ratio α thus satisfies the condition required by the approximate equations. Therefore, according to the coordinate in Fig. 1a, the velocity profile in rectangular microchannel is

$$v(y,z) = v_{ave}\left(\frac{m+1}{m}\right)\left(\frac{n+1}{n}\right) \\ \times \left[1 - \left(\frac{2y}{w_c}\right)^m\right]\left[1 - \left(\frac{2z}{d_c}\right)^n\right] \tag{9}$$

where v_{ave} is the average velocity in the x direction.

3.2 Numerical simulation

We developed a method to simulate the trajectory of the magnetic particles. First, finite element software package FEMM (Meeker 2010) was used to simulate the magnetic field in the microfluidic channel. A custom-written Matlab program was employed to determine the particle position with respect to time by Newton's second law. Magnetic force distribution on the particle as a function of space can also be calculated to understand the effects of various factors on the particle trajectory and separation performance. The initial particle positions in the simulations have the same z coordinate as the experiment. In the experiment measurement, particles near the centerline of microfluidic channel were selected; and all sample particles were almost on the same z plane to ensure consistent and meaningful comparisons. Previous studies have suggested that the gravity can play an important role in determining the particle motions when the particles are heavier than the surrounding liquid (Samiei et al. 2015; Nejad et al. 2015). However, in our study, the effect of gravity can be safely neglected because the particle velocity in the z direction is negligible compared to the velocities in the x and y direction. The estimation of the velocity scales suggests that the velocity in the z direction is at least 100 times smaller than those in the x and y direction. It is thus reasonably accurate to assume that the particle will stay in the same z plane during the process flowing through the fluid channel. As a result, 2-D simulations can be used as long as the particle location in z direction is known. In the comparison between the simulations and experiments, the z location was first obtained from experiment measurement and subsequently used in the 2-D simulations.

Magnetic field The geometry of the same size with experiment was constructed in FEMM. The material of microfluidic channel was set as air. The relative magnetic permeability of the microstructure was set according to the mass ratio of the iron–PDMS composite, and the values were derived from the experimental data as reported in the literature (El-Nashar et al. 2006; Li et al. 2011; Faivre et al. 2014). At a mass ratio of 2:1, $\mu_r = 1.706$, and at a mass ratio of 1:1, $\mu_r = 1.45$. The NdFeB permanent magnets used in the experiment have a grade of 42 MGOe, and the correct coercivity H_c was used in FEMM accordingly.
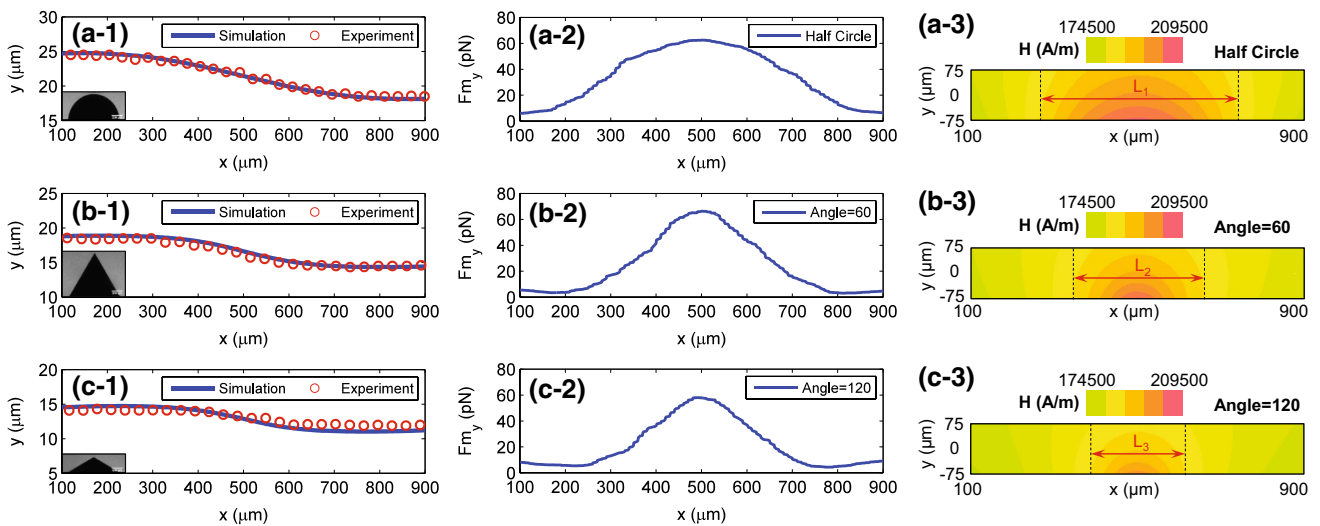
Fig. 2 Effect of the microstructure shapes. **a-1**, **b-1** and **c-1** compare the experimental (*symbols*) and simulated particle trajectories (*lines*) with the *half circle*, 60° triangle, and 120° triangle microstructures; **a-2**, **b-2**, and **c-2** are the corresponding F_{my} from simulations; **a-3**, **b-3**, and **c-3** are the corresponding magnetic field intensity in the microfluidic channel. The flow rate is $Q_1 = Q_2 = 1.5\,\mu L/min$, the width of microfluidic channel is $w_c = 150\,\mu m$, and the mass ratio of iron–PDMS is 2:1

The simulation domain was set as at least five times of the microdevice size. The boundary condition of magnets, microfluidic channel, and microstructure channel was set as a mixed one to solve the static Maxwell's equations (Meeker 2010). The magnetic field intensity H_x and H_y were exported by a script written in Lua programming language and saved in a text file. The magnetic field data was later imported to the Matlab program to calculate the magnetic force through Eq. (2).

Particle trajectory The particle motion is calculated by Newton's second law (Furlani and Ng 2006; Zhu et al. 2010, 2012). At each time instance, the forces on the particle, $\mathbf{F}_m$ and $\mathbf{F}_d$, and the corresponding particle acceleration are calculated,

$$a_x = \frac{F_{dx} + F_{mx}}{m_p}, \tag{10}$$

$$a_y = \frac{F_{dy} + F_{my}}{m_p}. \tag{11}$$

The instantaneous position of a particle, r_x and r_y, are then computed over time by

$$r_x = x_0 + v_{0x}t + \frac{1}{2}a_x t^2, \tag{12}$$

$$r_y = y_0 + v_{0y}t + \frac{1}{2}a_y t^2, \tag{13}$$

where x_0 and y_0 are the initial location of the particle, $v_{0x} = v_{0y} = 0$ are the initial particle velocity, t is time, F_{dx} and F_{dy} are the x and y components of the hydrodynamic

drag force, F_{mx} and F_{my} are the x and y components of the magnetic force, and m_p is the mass of the particle.

4 Results and discussion

When the iron–PDMS microstructure is placed between two external permanent magnets, it induces localized and strong forces on the magnetic particles in the direction perpendicular to the pressure-driven fluid flows. The separation of particles thus depends on the magnetic forces. According to Eq. (2), the magnetic forces have a strong dependence on the magnetic field and its gradient, which, in turn, are affected by the shape of iron–PDMS microstructure, the mass ratio of iron–PDMS composite, and the width of the microfluidic channel. Additionally, the flow rate in the fluid channel affects the time experienced by the magnetic particle (residence time t_r) and thus the vertical deflection in the y-direction. In the following sections, systematic experiments and numerical simulations were used to examine the influence of these factors on the separation performance.

4.1 Effect of microstructure shape

The effect of iron–PDMS microstructure shapes on the particle transport is presented in this section. The three shape styles are half circle, 60° triangle, and 120° triangle, as shown in Fig. 2a-1, b-1, c-1. All of microstructures were fabricated with the same base length of 1000 μm and were positioned at $w_g = 60\,\mu m$ away from the fluidic channel.

Figure 2a-1, b-1 and c-1 compares the experimental and simulated particle trajectories due to the three soft magnetic microstructures, respectively. It is evident from the comparison that the experimental trajectories were in good agreement with the simulation. The superparamagnetic particles were deflected toward the lower side of microfluidic channel because of the magnetic force induced by the iron–PDMS microstructures.

Note that the initial positions (y_0) of the particles in were slightly different in Fig. 2a-1, b-1, and c-1. This difference was due to the practical constraints of the experiments where there were limited number of particles. For initial positions y_0 between 15 and 25 μm, the experimental data points were most abundant and could be found for all experiment conditions. For this reason, we focused on y_0 between 15 and 25 μm in order to make systematic assessment of the effects of microstructure shape, mass ratio of iron powers, and channel width. To ensure consistency, we used numerical simulations to evaluate the effect of y_0. For initial positions $15\,\mu\text{m} \leq y_0 \leq 25\,\mu\text{m}$, the resulted $\Delta y = y_1 - y_0$ changed by only 5.11, 5.80 and 6.61% for the half circle, 60 and 120° triangles, respectively. In all experimental analysis, we ensured the condition $15\,\mu\text{m} \leq y_0 \leq 25\,\mu\text{m}$. The comparisons for different experiment conditions are thus considered consistent and meaningful.

Among the three shapes investigated, the half circle microstructure resulted in the largest deflection. This can be understood by the vertical magnetic force F_{my} calculated from the numerical simulations, as shown in Fig. 2a-2, b-2, and c-2. While the maximum F_{my} was about the same at 70 pN, the half circle iron–PDMS microstructure had a wider acting range in the channel to deflect the particle toward the lower wall side faster. To visualize the influence range, the distributions of magnetic field strength $|H|$ are plotted in Fig. 2a-3, b-3, and c-3. For the same variation range of $|H|$, the half circle structure had a wider influence range (L_1), which is larger than those due to the 60° (L_2) and 120° (L_3) triangles.

When varying the average flow velocity, the deflection distance $\Delta y = y_1 - y_0$ decreases with increasing flow velocity for all microstructures, as shown in Fig. 3. The vertical deflection distance is the result of the competition of the vertical magnetic force and the viscous drag force. With an increasing flow velocity and a larger drag force, the residence time, t_r, of the particle within the influence range of F_{my} becomes shorter. Despite the same magnetic force (the same vertical velocity), Δy becomes smaller because of the shorter residence time t_r. For all velocities examined, the half circle had the best performance on particle deflection in the y-direction, since F_{my} effect range was wider, which had been discussed before; 60° triangle worked better than 120° triangle for the same reason.
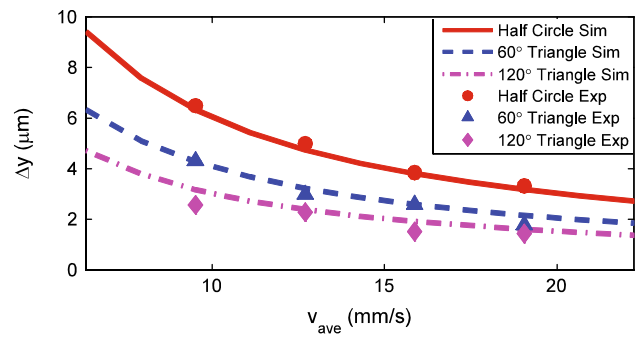

Fig. 3 Effect of average flow velocity. Δy at different average flow velocity v_{ave} under three different microstructures. For all experiments and simulations, $y_0 \approx 20\,\mu$m, iron/PDMS (w/w)=2, $w_c = 150\,\mu$m. *Lines* and *symbols* represent simulation and experimental data, respectively
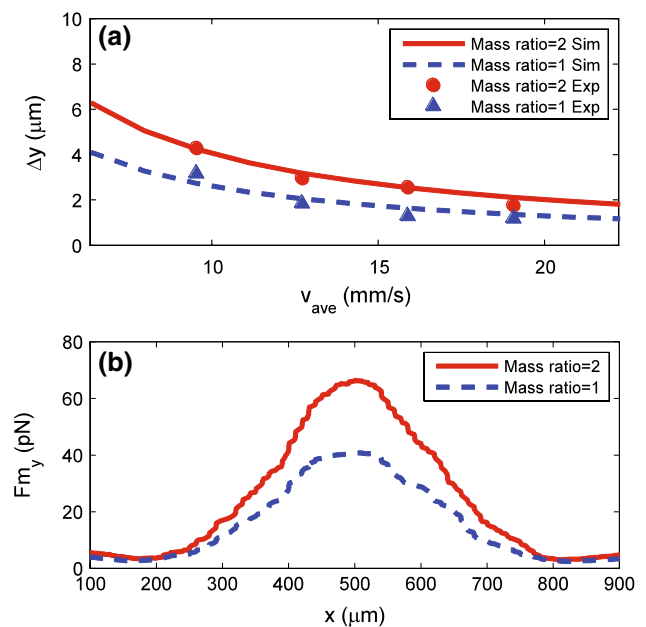

Fig. 4 Effect of the iron mass ratio of the iron–PDMS composite. **a** Δy at different average flow velocity v_{ave} with the 60° triangle microstructure; *lines* and *symbols* represent simulation and experimental data, respectively. **b** the corresponding magnetic force F_{my} from the simulations when $v_{ave} = 9.52$ mm/s. The width of microfluidic channel is 150 μm in all experiments and simulations

4.2 Effect of iron mass ratio of the composite

In addition to the shapes, the mass ratio of the iron powder can effect the separation performance, because it influences the magnetic permeability of the composite and the induced magnetic field. In this study, the mass ratio of between the iron and PDMS were varied from 1:1 to 2:1. In Fig. 4, the microstructure was the 60° triangle in order to study the effect of the mass ratio of iron powders. Figure 4a shows that microstructure of iron/PDMS (w/w) = 2 deflected

the particles by a larger displacement in the y direction for all the average flow velocity v_{ave} than the microstructures made of iron/PDMS (w/w) = 1. This is because the composite of iron/PDMS (w/w) = 2 had a larger magnetic permeability $\mu_r = 1.706$, while the microstructures of iron/PDMS (w/w) = 1 had a smaller permeability, $\mu_r = 1.45$ (Faivre et al. 2014. Therefore, a larger mass ratio of iron can produce stronger magnetic field gradients and larger magnetic forces to separate magnetic particles. Figure 4b illustrates the magnetic force in the y direction acting on the 5 μm particles when $v_{ave} = 9.52$ mm/s. As can be seen in Fig. 4b, the microstructure made of iron–PDMS (w/w) = 2 had both a larger force and a wider acting range on the magnetic particle, leading to larger deflection of the particle toward the lower wall side.

Despite a small change from $\mu_r = 1.45$ to $\mu_r = 1.706$, the resultant forces almost doubled, as shown in Fig. 4b. A mass ratio of 3 or larger would have an even better sorting performance on the magnetic particles. However, the iron–PDMS mixture with mass ratio of 3 was too viscous to be injected into the microstructure channels used in this study. If a larger mass ratio and a large force are needed, the microstructures can be designed to have wider cross-sectional areas to allow the injection of the more viscous iron–PDMS mixture.

4.3 Effect of microfluidic channel width

The width of microfluidic channel, w_c, influences the particle separation as well. When w_c changes, the distance between the particle to the microstructure will be different and thus the magnetic forces will be different. For a meaningful assessment of the effect of w_c, the flow rate Q_t was kept the same. In addition, the initial positions of the particles, y_0 were chosen to have the same relative position with respect to the channel width, that is the same $\frac{y_0}{w_c}$ for all cases. In accordance, $\frac{\Delta y}{w_c}$ will be the measurement of the separation performance.

Unlike the previous two factors (shape and mass ratio of iron–PDMS) that only affect the magnetic force, the channel width, w_c affects both the drag force and the magnetic force. When w_c decreases, the pressure-driven velocity and drag force increase and thus the particle residence time t_r will decrease. In the meantime, the particles are situated relatively closer to the iron–PDMS microstructure and thus the magnetic force will increase. These two effects have opposite influences on the particle deflection. To understand the combined effect of w_c, extensive simulations (w_c from 50 to 750 μm) were conducted. It can be found in Fig. 5a that under the condition of $w_c = 500$ and 750 μm, the deflection was so small, resulting in little separation considering the relatively large width of the fluidic channel. Although the deflection of $w_c = 50$ μm was large enough, it
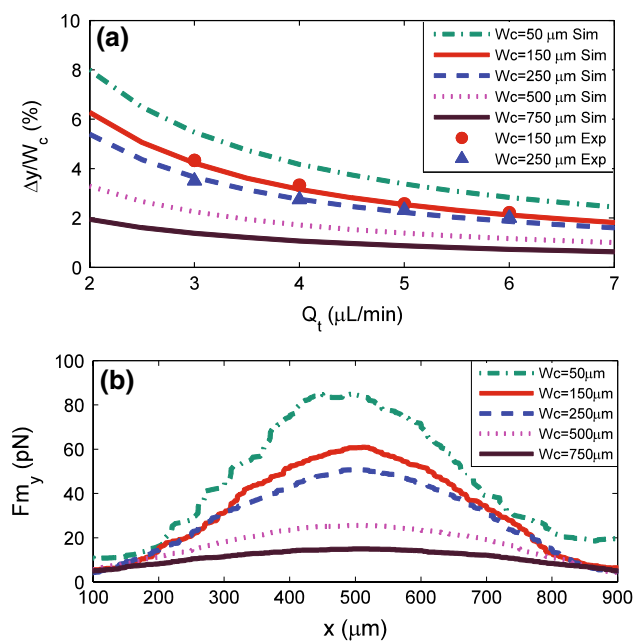

Fig. 5 Effect of the width of the microfluidic channel. **a** $\Delta y = y_1 - y_0$ at different flow rates. *Lines* and *symbols* represent simulation and experimental data, respectively. **b** the corresponding F_{my} from the simulations. The flow rate is $Q_1 = Q_2 = 1.5$ μL/min. The particles all have approximately the same initial relative positions, $\frac{y_0}{(W_c/2)} = \frac{4}{15}$. The microstructure is half circle, and has a iron mass ratio iron/PDMS (w/w)=2

was beyond the ability of the current fabrication technique. Nevertheless, these cases were calculated to show the trend of $\frac{\Delta y}{w_c}$ vs Q_t for each width. Experimental measurements and simulations were compared by choosing $w_c = 150$ and 250 μm, and showed good agreement, as shown in Fig. 5a.

The experiments and simulations showed that the value of $\frac{\Delta y}{w_c}$ became larger when the microfluidic channel became narrower. This trend means that the effect of increasing F_{my} is more dominant over the effect of decreasing residence time. The magnetic force F_{my} showed a dramatic change when w_c was varied in Fig. 5b. As the channel width decreases, the rate of increase of F_{my} is faster than the linear rate of decrease of the residence time t_r, which is inversely proportional to the channel width.

4.4 Separation with multiple microstructures

In the above sections, it has been showed that single microstructure can result in the y-direction displacement of particles. To further enhance the separation, multiple microstructures were designed to test the practical use of our proposed devices. The half circular structure was chosen because of its superior performance, as shown in Fig. 6a. The microfluidic channels had a width 150 μm and were placed next to multiple (total 11) connected half circle
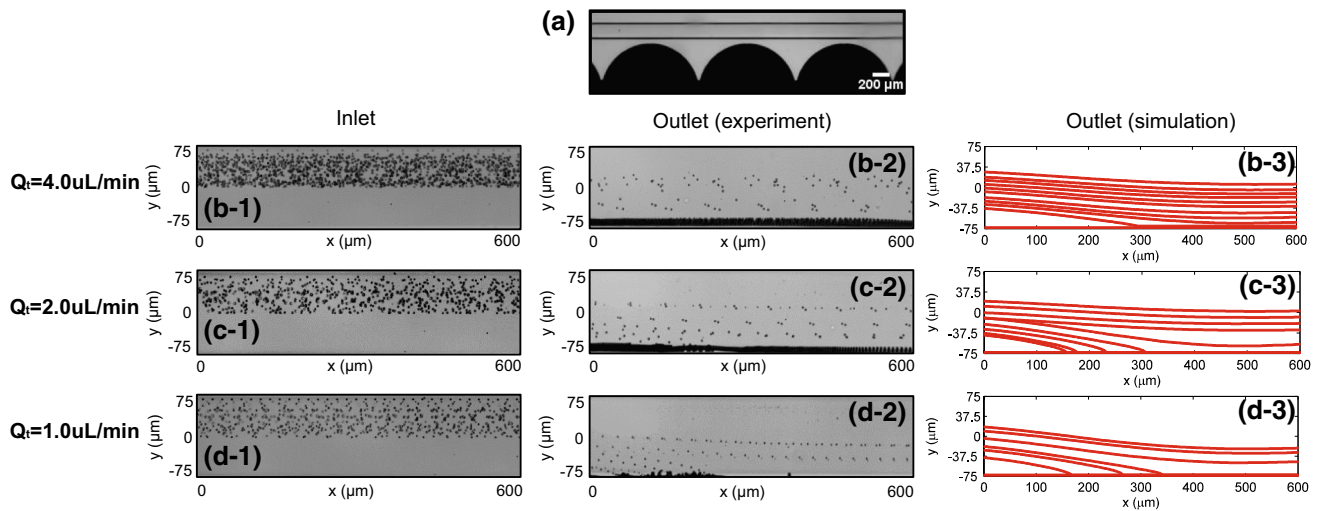
Fig. 6 Separation of magnetic particles with multiple iron–PDMS microstructures. **a** image of connected half circle iron–PDMS microstructure. **b-1**, **c-1**, and **d-1** are the superposed images at the inlet of the microfluidic channels at different flow rates. **b-2**–**d-2**, and **b-3**–**d-3** are the corresponding images at the outlets

microstructures made of iron/PDMS (w/w) = 2. Solutions with magnetic particles entered into the top half of the fluid channel, as shown in Fig. 6b-1, c-1, and d-1. The magnetic particles were pulled toward the lower half, as shown in the superposed images captured at the channel outlets in Fig. 6 b-2, c-2, and d-2.

In practical applications, the magnetic particles occupy the entire upper half of the channel at the inlet. To achieve a complete separation, the particles near the top channel wall must be deflected by a distance of the half channel width. As can be seen in Fig. 6, complete separation was achieved at a total flow of 1.0 μL/min. The simulated particle trajectories agreed well with the experimental data.

In Fig. 6b-2, c-2, d-2, it seems that a higher flow rate would be likely to collect more particles than a slow flow rate. This seems counter-intuitive, but can be explained as follows. At lower flow rate, some of the magnetic particles can be deflected to the channel wall before reaching to the outlet. When magnetic particles were attracted to the bottom surface, the friction between particles and channel wall would be large and the particles moved slowly to the outlet. When the flow rate was small as shown in Fig. 6d-2, most particles were absorbed to the bottom surface and stopped at the wall before they arrived at the outlet due to the weak pressure-driven flow. When the flow rate was large as shown in Fig. 6b-2, most particles were attracted to the wall just before the outlet. Further, because the pressure-driven flow was strong enough to overcome the friction, more particles appeared at the channel outlet; additionally, the superposed images in Fig. 6b-2, c-2, d-2 were obtained with image stacks of the same time duration. That also means more particles moved through the channel when the

flow rate was larger. Aggregated particles may have effect on the distribution of magnetic field distribution, if they are large enough compared to the microstructures. However, in our study, the particle solution was dilute; therefore, the aggregated particles were small compared with the microstructures which were several hundred microns.

The viscosity of the solution used in this study was 5 mPa·s, about 4–5 times more viscous than common aqueous biological solutions. Therefore, the throughput would be a few times higher when the device is used with less viscous solutions. Moreover, the throughput can be further improved with multiple parallel channels. Our proposed technique will be particularly useful for high-throughput particle/cell separation with short durations(e.g., minutes to hours), and during these operation time frames no iron particles can permeate into main microchannel.

5 Conclusions

We proposed and demonstrated a simple and low-cost method for fabricating microfluidic devices for enhanced separation of magnetic particles. The microfluidic devices integrated soft magnetic microstructures next to microfluidic channels, with a distance of tens of micrometers. The induced magnetic fields and gradients resulted in strong forces that can deflect magnetic particles perpendicular to the pressure-driven flow. By simulating the magnetic fields and computing the corresponding magnetic forces, a numerical simulation method was developed to predict the particle trajectory and showed good agreement with the experimental data.

Systematic experiments and simulations were conducted to study the effect of several relevant factors on the separation of superparamagnetic particles, including the microstructure shape, the mass ratio of the iron–PDMS microstructure, and the microfluidic channel width. Important findings include: First, half circular iron–PDMS microstructure causes larger deflections of the particles than isosceles triangle shaped structures; second, a larger mass ratio of the iron–PDMS composite results in larger magnetic forces; third, narrow microfluidic channels separate magnetic particles more efficiently than wider channels when operating at the same flow rate.

Our approach presents an efficient and simple method to separate magnetic particles in microfluidics. Compared to the existing techniques, the current method will reduce the chance of contamination to cells because the microstructures are located outside the fluid channel. In addition, the distance between the microfluidic channel and the microstructure channel can be adjusted to control the magnetic forces. As such, the proposed microfluidic devices are promising and have potential in areas such as high-throughput separation of biological cells tagged with micro/nano-magnetic particles.

References

Abramoff M, Magalhes P, Ram S (2004) Image processing with imagej. Biophoton Int 11(7):36–41

Balasubramanian P, Lang J, Jatana K, Miller B, Ozer E, Old M, Schuller D, Agrawal A, Teknos T, Summers JT, Lustberg M, Zborowski M, Chalmers J (2012) Multiparameter analysis, including emt markers, on negatively enriched blood samples from patients with squamous cell carcinoma of the head and neck. PLoS One 7(7):e42048. doi:10.1371/journal.pone.0042048

Deng T, Prentiss M, Whitesides G (2002) Fabrication of magnetic microfiltration systems using soft lithography. Appl Phys Lett 80(3):461–463

Derec C, Wilhelm C, Servais J, Bacri JC (2010) Local control of magnetic objects in microfluidic channels. Microfluid Nanofluid 8(1):123–130

Do J, Choi JW, Ahn C (2004) Low-cost magnetic interdigitated array on a plastic wafer. IEEE Trans Mag 40(4 II):3009–3011

El-Nashar D, Mansour S, Girgis E (2006) Nickel and iron nano-particles in natural rubber composites. J Mater Sci 41(16):5359–5364

Engel A, Friedrichs R (2002) On the electromagnetic force on a polarizable body. Am J Phys 70(4):428–432

Faivre M, Gelszinnis R, Degouttes J, Terrier N, Rivière C, Ferrigno R, Deman AL (2014) Magnetophoretic manipulation in microsystem using carbonyl iron-polydimethylsiloxane microstructures. Biomicrofluidics 8(5):054103

Furlani EP, Ng KC (2006) Analytical model of magnetic nanoparticle transport and capture in the microvasculature. Phys Rev E Stat Nonlinear Soft Matter Phys 73(6):061919. doi:10.1103/PhysRevE.73.061919

Furlani E, Sahoo Y (2006) Analytical model for the magnetic field and force in a magnetophoretic microsystem. J Phys D Appl Phys 39(9):1724–1732

Ganatos P, Weinbaum S, Pfeffer R (1980) A strong interaction theory for the creeping motion of a sphere between plane parallel boundaries. part 1. perpendicular motion. J Fluid Mech 99:739–753

Gelszinnis R, Faivre M, Degouttes J, Terrier N, Ferrigno R, Deman AL (2013) Magnetophoretic manipulation in microsystem using i-pdms microstructurs, vol 1. In: 17th international conference on miniaturized systems for chemistry and life sciences, pp 146–148

Gijs M (2004) Magnetic bead handling on-chip: new opportunities for analytical applications. Microfluid Nanofluid 1(1):22–40

Gijs MA, Lacharme F, Lehmann U (2009) Microfluidic applications of magnetic particles for biological analysis and catalysis. Chem Rev 110(3):1518–1563

Han KH, Bruno Frazier A (2004) Continuous magnetophoretic separation of blood cells in microdevice format. J Appl Phys 96(10):5797–5802

Hejazian M, Li W, Nguyen NT (2015) Lab on a chip for continuous-flow magnetic cell separation. Lab Chip 15(4):959–970

Inglis DW, Riehn R, Austin R, Sturm J (2004) Continuous microfluidic immunomagnetic cell separation. Appl Phys Lett 85(21):5093–5095

Krishnan GP, Leighton DT (1995) Inertial lift on a moving sphere in contact with a plane wall in a shear flow. Phys Fluids 7(11):2538–2545

Li J, Zhang M, Wang L, Li W, Sheng P, Wen W (2011) Design and fabrication of microfluidic mixer from carbonyl iron–PDMS composite membrane. Microfluid Nanofluid 10(4):919–925

Lin YA, Wong TS, Bhardwaj U, Chen JM, McCabe E, Ho CM (2007) Formation of high electromagnetic gradients through a particle-based microfluidic approach. J Micromech Microeng 17(7):1299

Lund-Olesen T, Bruus H, Hansen M (2007a) Quantitative characterization of magnetic separators: comparison of systems with and without integrated microfluidic mixers. Biomed Microdevices 9(2):195–205

Lund-Olesen T, Dufva M, Hansen M (2007b) Capture of dna in microfluidic channel using magnetic beads: increasing capture efficiency with integrated microfluidic mixer. J Magn Magn Mater 311(1 SPEC. ISS.):396–400

McDonald J, Duffy D, Anderson J, Chiu D, Wu H, Schueller O, Whitesides G (2000) Fabrication of microfluidic systems in poly(dimethylsiloxane). Electrophoresis 21(1):27–40

Meeker D (2010) Finite element method magnetics. FEMM 4:32

Nejad HR, Samiei E, Ahmadi A, Hoorfar M (2015) Gravity-driven hydrodynamic particle separation in digital microfluidic systems. RSC Adv 5:35,966–35,975

Nguyen NT (2012) Micro-magnetofluidics: interactions between magnetism and fluid flow on the microscale. Microfluid Nanofluid 12(1–4):1–16

Nguyen VC, Pho QH (2014) Preparation of chitosan coated magnetic hydroxyapatite nanoparticles and application for adsorption of reactive blue 19 and Ni2+ ions. Sci World J 2014:273082. doi:10.1155/2014/273082

Pamme N (2006) Magnetism and microfluidics. Lab Chip Miniat Chem Biol 6(1):24–38

Rida A, Gijs M (2004) Manipulation of self-assembled structures of magnetic beads for microfluidic mixing and assaying. Anal Chem 76(21):6239–6246

Safarik I, Safarikova M (1999) Use of magnetic techniques for the isolation of cells. J Chromatogr B Biomed Sci Appl 722(1–2):35–53

Safarik I, Safarikova M (2004) Magnetic techniques for the isolation and purification of proteins and peptides. BioMagn Res Technol 2:7

Samiei E, Rezaei Nejad H, Hoorfar M (2015) A dielectrophoretic-gravity driven particle focusing technique for digital microfluidic systems. Appl Phys Lett 106(20):204101

Shah RK, London AL, Irvine TF, Hartnett JP (1978) Laminar flow forced convection in ducts. Academic Press, Cambridge

Shenkman R, Chalmers J, Hering B, Kirchhof N, Papas K (2009) Quadrupole magnetic sorting of porcine islets of langerhans. Tissue Eng Part C Methods 15(2):147–156

Siegel AC, Shevkoplyas SS, Weibel DB, Bruzewicz DA, Martinez AW, Whitesides GM (2006) Cofabrication of electromagnets and microfluidic systems in poly(dimethylsiloxane). Angew Chem Int Ed 45(41):6877–6882

Smistrup K, Kjeldsen B, Reimers J, Dufva M, Petersen J, Hansen M (2005) On-chip magnetic bead microarray using hydrodynamic focusing in a passive magnetic separator. Lab Chip Miniat Chem Biol 5(11):1315–1319

Smistrup K, Bu M, Wolff A, Bruus H, Hansen MF (2008) Theoretical analysis of a new, efficient microfluidic magnetic bead separator based on magnetic structures on multiple length scales. Microfluid Nanofluid 4:565–573

Staben ME, Zinchenko AZ, Davis RH (2003) Motion of a particle between two parallel plane walls in low-reynolds-number poiseuille flow. Phys Fluids 15(6):1711–1733

Svoboda J (2001) A realistic description of the process of high-gradient magnetic separation. Miner Eng 14(11):1493–1503

Tan SH, Semin B, Baret JC (2014) Microfluidic flow-focusing in ac electric fields. Lab Chip 14(6):1099–1106

Verpoorte E (2003) Beads and chips: new recipes for analysis. Lab Chip 3(4):60N–68N

Watson J (1973) Magnetic filtration. J Appl Phys 44(9):4209–4213

White FM (1991) Viscous fluid flow, 2nd edn. McGraw-Hill, New York

Xia N, Hunt T, Mayers B, Alsberg E, Whitesides G, Westervelt R, Ingber D (2006) Combined microfluidic-micromagnetic separation of living cells in continuous flow. Biomed Microdevices 8(4):299–308

Yang L, Lang J, Balasubramanian P, Jatana K, Schuller D, Agrawal A, Zborowski M, Chalmers J (2009) Optimization of an enrichment process for circulating tumor cells from the blood of head and neck cancer patients through depletion of normal cells. Biotechnol Bioeng 102(2):521–534

Zhang Z, Zhou R, Brames DP, Wang C (2015) A low-cost fabrication system for manufacturing soft-lithography microfluidic master molds. Micro Nanosyst 7(1):4–12

Zhou R, Wang C (2015) Acoustic bubble enhanced pinched flow fractionation for microparticle separation. J Micromech Microeng 25(8):084005. doi:10.1088/0960-1317/25/8/084005

Zhu J, Liang L, Xuan X (2012) On-chip manipulation of nonmagnetic particles in paramagnetic solutions using embedded permanent magnets. Microfluid Nanofluid 12(1–4):65–73

Zhu T, Marrero F, Mao L (2010) Continuous separation of non-magnetic particles through negative magnetophoresis inside ferrofluids. In: 2010 IEEE 5th international conference on nano/micro engineered and molecular systems, pp 1006–1011